



CHORUS

This is the accepted manuscript made available via CHORUS. The article has been published as:

Nonresonant Raman scattering in extremely correlated Fermi liquids

Peizhi Mai and B. Sriram Shastry

Phys. Rev. B **98**, 115101 — Published 4 September 2018

DOI: [10.1103/PhysRevB.98.115101](https://doi.org/10.1103/PhysRevB.98.115101)

Non-resonant Raman Scattering in Extremely Correlated Fermi Liquids

Peizhi Mai and B. Sriram Shastry

Physics Department, University of California, Santa Cruz, CA 95064

(Dated: August 1, 2018)

We present theoretical results for the optical conductivity and the non-resonant Raman susceptibilities for three principal polarization geometries relevant to the square lattice. The susceptibilities are obtained using the recently developed extremely correlated Fermi liquid theory for the 2-dimensional t - t' - J model, where t and t' are the nearest and second neighbor hopping. Our results sensitively depend on t , t' . By studying this quartet of related dynamical susceptibilities, and their dependence on t , t' , doping and temperature, we provide a useful framework of interpreting and planning future Raman experiments on strongly correlated matter.

I. INTRODUCTION

Inelastic or Raman scattering of electrons by photons (e - γ) in strongly correlated systems is of considerable current interest. The scattering intensity, given by the Kramers-Heisenberg formula¹, consists of a resonant and a non-resonant piece. The non-resonant piece depends only on the energy transfer, unlike the resonant piece that also depends on the incident energy, and is the focus of this work. In typical weakly correlated metals, this contribution is confined to a small energy window of a few meV ^{2,3}. Raman scattering theory metals, if based solely on density fluctuations, would give a vanishing contribution as $q \rightarrow 0$ due to the conservation law in that limit. The early works of Ref. [2] and Ref. [4] showed that non-parabolic bands lead to the coupling of light to a non-conserved operator (the stress tensor operators discussed below), rather than the density. These operators are exempt from conservation laws that govern the density, and therefore can lead to non-resonant Raman scattering.

Recent experiments⁵⁻¹⁷ in strongly correlated metallic systems, such as the High Tc superconductors have thrown up further complexity to challenge to our understanding. It is found that the scattering is q independent and extends over a much larger energy range $\mathcal{O}(eV)$, and is also observed to have a complex T dependence^{5-7,10,14}. To explain these a systematic reformulation of light scattering in narrow band systems was developed in Ref. [18-23]. Shastry and Shraiman (SS) Ref. [18,19] developed a theory of Raman scattering in Mott-Hubbard systems using the Hubbard model, where nonparabolicity of bands is built in correctly, so that the conservation law concerns are taken care of. However the large energy spread of the non-resonant signals remains unaccounted for. It cannot arise from quasi-particles in Fermi liquids, and hence SS argued that a large contribution from the incoherent background of the electron spectral function is required to explain the data (see e.g.^{5,6}). This qualitative argument is not fine enough to explain or predict differences in backgrounds in different geometries. The latter remains an unresolved problem, and is the focus of the present work.

Progress towards a solution at the microscopic level

has been slow since a suitable theory in 2-dimensions displaying such a phenomenon has been lacking so far. In this work we apply the recently developed extremely correlated Fermi liquid theory (ECFL)^{24,29} to calculate the Raman cross sections using the k -dependent bare vertices of Ref. [18,19]. This theory provides a framework for controlled calculations in the t - J model, a prototypical model for very strong correlations, and a limiting case of the Hubbard model. The theory has been successfully benchmarked against essentially exact results in $d = 0$ ²⁶, $d = 1$ ²⁷ as well as $d = \infty$ ²⁸. A recent application of the theory to the physically important case of $d = 2$ in Ref. [29,30] gives detailed results for the spectral functions and the resistivity ρ in the t - t' - J model, with nearest and second neighboring hopping. The state obtained in ECFL at low hole densities has a very small quasi-particle weight $Z \ll 1$. A significant result is that the temperature dependence of resistivity is non-quadratic already at $T \sim 100K$ for low hole doping.

In this work we apply the solution found in Ref. [29,30] to compute the Raman scattering, in three standard polarization configuration channels A_{1g}, B_{1g}, B_{2g} defined below³¹. The results are applicable to either electron doping or hole doped cuprates by choosing the sign of t' , and possibly applies to other strongly correlated systems as well. Following SS, we also compare the Raman conductivities with the optical conductivity, and shall focus on the quartet of these results on various values of material parameters.

The utility of comparing the optical conductivity with the Raman response requires a comment. SS^{18,19} suggested that this comparison is useful, since these are exactly related in a limiting situation of $d = \infty$. Further in $d = 2, 3, \dots$, one often calculates the response within the bubble diagrams, where again these are related. In the bubble approximation, also used in the present work, one evaluates the current-current and related correlation functions by retaining only the lowest order $\chi_{JJ} \sim \sum_k (\gamma_k)^2 G(k)G(k)$ (i.e. bubble) terms with dressed Greens functions and suitable bare vertices γ . While this calculation misses a contribution due to the renormalization of one of the bare vertices $\gamma \rightarrow \Gamma$, it is hard to improve on this already difficult calculation for strong correlations, since G is highly non-trivial. An ex-

ception is the special case of $d \rightarrow \infty$, where the vertex corrections vanish. Within the bubble scheme, the bare Raman and current vertices are different while everything else is the same. Therefore one should be able to relate the two experimental results and explore the differences arising from the bare vertices. The ‘‘pseudo-identity’’ of the transport and Raman resistivities have been explored experimentally in Ref. [8] and finds some support. In this work we use the correct bare vertices in the different geometries to explore the various Raman resistivities to refine the theory. These different bare vertices have a different dependence on the hopping parameters t, t' and the calculations reflect these in specific and experimentally testable ways.

The neglect of vertex corrections also leads to a relationship between various Raman susceptibilities at finite ω . In the experiments of Ref. [6], the same quartet of susceptibilities have been studied and found to have a roughly similar scale for their ω dependence, although the curve shapes are distinct. On the theoretical side, one interesting aspect of the results of Ref. [29,30] is that the Fermi surface *shape* remains very close to that of the non-interacting tight binding model, while of course conserving the area. Thus the Dyson self energy is a weak function of \vec{k} , unlike the strong dependence in 1-dimension²⁷. This fact implies that the vertex corrections, while nonzero, are modest.

II. THE RAMAN AND CURRENT VERTICES

We use the t - t' - J model with a tight binding dispersion²⁹ on the square lattice $\varepsilon(k) = -2t[\cos(k_x) + \cos(k_y)] - 4t' \cos(k_x) \cos(k_y)$, and set the lattice constant $a_0 \rightarrow 1$. The photons modulate the Peierls hopping factors as $t_{ij} \rightarrow t_{ij} \exp\{ie/\hbar \int_i^j d\vec{r} \cdot \vec{A}\}$, and the second order expansion coefficients define the scattering operators. In this case they are

$$\hat{\mathcal{J}}_{\alpha,q} = \sum_{k\sigma} \mathcal{J}_{\alpha}(k) C_{k+\frac{1}{2}q,\sigma}^{\dagger} C_{k-\frac{1}{2}q,\sigma}, \quad (1)$$

where α is a composite index determined by the in-out polarizations of the photon. With that the vertex \mathcal{J}_{α} for the three main Raman channels are

$$\begin{aligned} A_{1g} : \quad \mathcal{J}_{A_{1g}}(k) &= 2t(\cos k_x + \cos k_y) + 4t' \cos k_x \cos k_y, \\ B_{1g} : \quad \mathcal{J}_{B_{1g}}(k) &= 2t(\cos k_x - \cos k_y), \\ B_{2g} : \quad \mathcal{J}_{B_{2g}}(k) &= -4t' \sin k_x \sin k_y, \\ xx : \quad \mathcal{J}_{xx}(k) &= 2 \sin k_x (t + 2t' \cos k_y). \end{aligned} \quad (2)$$

The definition of $\alpha = xx$ corresponds to the particle current along x . It integrates the charge current into the same scheme as the Raman scattering. It is interesting that the B_{2g} vertex is independent of t , and is solely governed by t' . The vertex B_{1g} is complementary given its independence of t' . These geometries sample different parts of k space in interesting ways due to their different \vec{k} dependences.

We next define the calculated variables, and display the results for them from computations based on the spectral functions found in Ref. [29,30]. Results in the $\omega = 0$ DC limit and also at finite ω are shown. Finally we discuss the results and their significance.

III. RAMAN AND CHARGE SUSCEPTIBILITIES

We summarize the formulas for the (non-resonant) Raman susceptibility, and in the spirit of Ref. [18,19] also define a *Raman conductivity and resistivity* in analogy as follows

$$\chi_{\alpha}(q, z) = \sum_{nm} \frac{p_n - p_m}{\epsilon_m - \epsilon_n - z} \times \left| \left(\hat{\mathcal{J}}_{\alpha,q} \right)_{n,m} \right|^2, \quad (3)$$

where p_n the probability of the state n . For visible light since $qa_0 \ll 1$ and we set $q \rightarrow 0$. The (non-resonant) Raman intensity $\mathcal{I}_{\alpha}^{1-3,18,19}$ and the Raman conductivities^{18,19} are given by

$$\mathcal{I}_{\alpha}(0, \omega) = \frac{\chi_{\alpha}''(0, \omega)}{(1 - e^{-\beta\omega})}, \quad \sigma_{\alpha}(\omega) = \zeta_{\alpha} \frac{\chi_{\alpha}''(0, \omega)}{N_s \omega}, \quad (4)$$

with N_s the number of sites, $\zeta_{xx} = e^2$ accounting for the electric charge in the conductivity with all other $\zeta_{\alpha} = 1$. In the DC limit we define the Raman resistivities

$$\rho_{\alpha}(0) = \frac{N_s}{\zeta_{\alpha}} \frac{k_B T}{\mathcal{I}_{\alpha}(0, 0)} \quad (5)$$

where for $\alpha = xx$, ρ_{α} is the usual resistivity.

The ‘‘pseudo-identity’’, a statement of universality relating electrical transport and the DC limit of Raman intensities noted by SS in Ref. [18,19] is arrived at, if we assume that ρ_{α} has a similar T dependence for all α : $\mathcal{I}_{\alpha}(0, 0) \sim C_{\alpha} \frac{T}{\rho_{xx}(T)}$ C_{α} is an α -dependent constant. Thus a $\rho \sim T^{\sigma}$ behavior would give rise to a $T^{1-\sigma}$ behavior for the Raman intensity in all channels. We see below in Fig. (1) that this suggestion is true for the A_{1g} resistivity at hole dopings, but it needs to be adjusted to the different k -dependent filters that make the B_{1g} and B_{2g} channels different from the others. Thus the we limit the universality of the pseudo-identity in this work, and quantify the effects of the bare vertices in the relationship between the members of the quartet of susceptibilities.

Proceeding further using the bubble scheme we get the imaginary part of the dimensionless susceptibility $\bar{\chi}_{\alpha}''(0, \omega) \equiv \frac{c_0 \hbar}{N_s} \chi_{\alpha}''(0, \omega)$ as

$$\bar{\chi}_{\alpha}''(0, \omega) = \omega \langle \Upsilon(k, \omega) \mathcal{J}_{\alpha}^2(k) \rangle_k, \quad (6)$$

where $c_0 \sim 6.64 \text{\AA}$ is a typical interlayer separation²⁹. The angular average is $\langle A \rangle_k \equiv \frac{1}{N_s} \sum_k A(k)$ and the momentum resolved relaxation scale is

$$\Upsilon(k, \omega) = \frac{4\pi^2}{\omega} \int_{-\infty}^{\infty} dy \rho_G(k, y) \rho_G(k, y + \omega) [f(y) - f(y + \omega)].$$

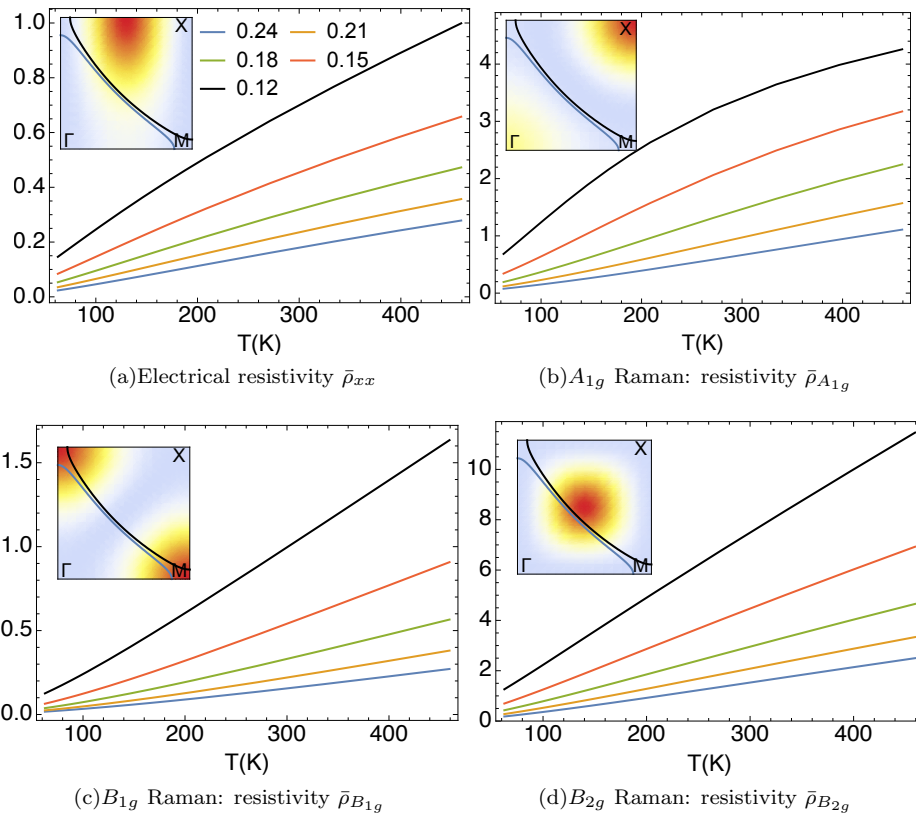


FIG. 1: Electrical and Raman resistivities from Eq. (5) at $t' = -0.2$ with varying hole doping δ , as marked. The T dependence of electrical resistivity and the A_{1g} resistivity concave-down at small δ , while the B_{1g} and B_{2g} resistivity are flat or concave-up. (Inset) The displayed Fermi surfaces at $\delta = .12, .24$ locate the maxima of $\Upsilon(k, \omega)$. The relevant squared vertices from Eq. (2) are shown as a heat map. The hot spots are movable by varying t' and t .

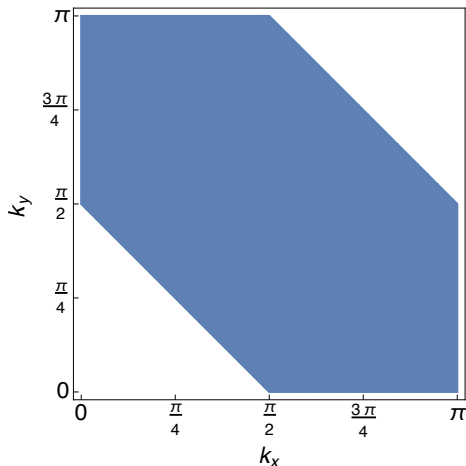


FIG. 2: 3 Shaded region for estimating average scale of vertices.

Here $\rho_G(k, \omega)$ is the electron spectral function. With $\rho_{1,\alpha} \equiv \frac{c_0 \hbar}{\zeta_\alpha}$, the corresponding dimensionless conductivity $\bar{\sigma}_\alpha(\omega) \equiv \rho_{1,\alpha} \times \sigma_\alpha(\omega)$ is given by

$$\bar{\sigma}_\alpha(\omega) = \langle \Upsilon(k, \omega) \mathcal{J}_\alpha^2(k) \rangle_k. \quad (7)$$

From Eqs (6) and (7), we can see $\bar{\chi}_\alpha''(0, \omega) = \omega * \bar{\sigma}_\alpha(\omega)$

IV. PARAMETER REGION

We explore how the variation of second neighbor hopping t' , doping δ and temperature T affects the quartet of conductivities and susceptibilities in the normal state. We focus on optimal doping or slightly overdoped cases from electron-doped (positive t') to hole-doped (negative t') systems. Our temperature region starts from 63K to a few hundred Kelvin.

V. DC LIMIT AND ELECTRICAL RESISTIVITY RESULTS:

Using the spectral function from second order ECFL theory, we calculate the dimensionless DC ($\omega \rightarrow 0$) electrical and Raman conductivities $\bar{\sigma}_\alpha$ from Eq. (7). The corresponding dimensionless resistivities are

$$\bar{\rho}_\alpha = \frac{1}{\bar{\sigma}_\alpha} = \frac{1}{\langle \Upsilon(k, 0) \mathcal{J}_\alpha^2(k) \rangle_k}, \quad (8)$$

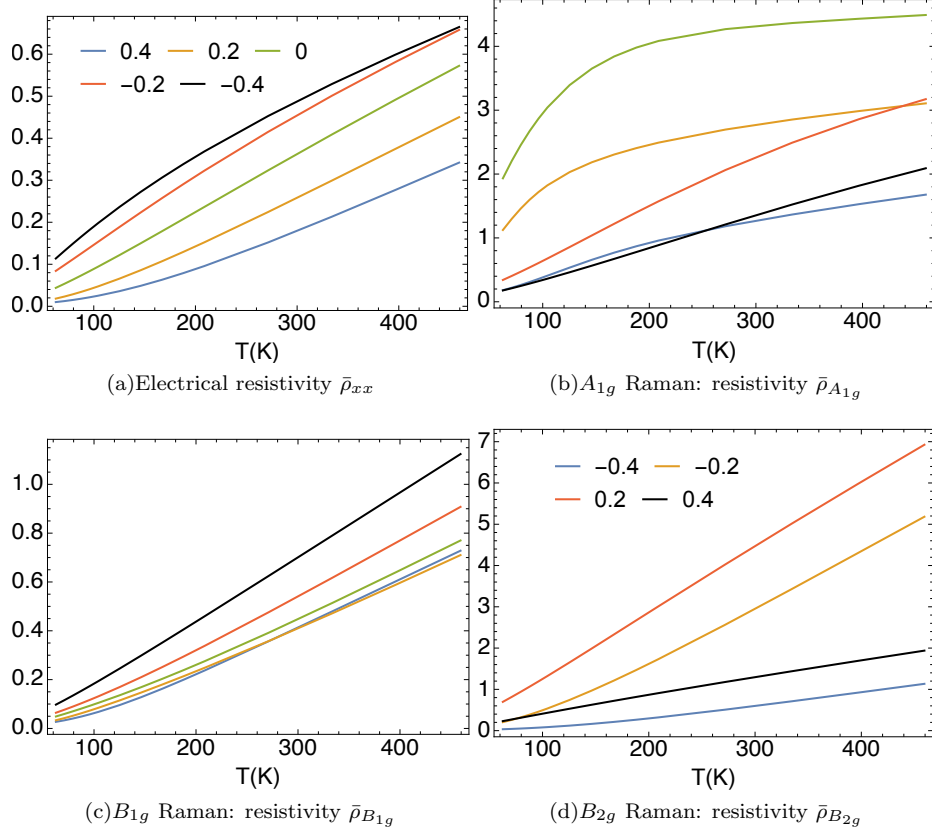


FIG. 3: Dimensionless $\bar{\rho}_{xx}$, taken from Ref. [29], $\bar{\rho}_{A_{1g}}$, $\bar{\rho}_{B_{1g}}$ and $\bar{\rho}_{B_{2g}}$ at $\delta = 0.15$ with varying second neighbor hopping t' , as marked (same legend for all subfigures). Ref. [8] displays data corresponding to the B_{1g} geometry.

The electrical resistivity in physical units is given by $\rho_{xx} = \bar{\rho}_{xx} \times \rho_{1,xx}$, with $\rho_{1,xx} = c_0 \frac{\hbar}{e^2} \sim 1.71 m \Omega \text{cm}^{29}$.

We calculate typical quantities for the three Raman geometries and the electrical conductivity from Eq. (2) as a set of quartets below. The comparison of the figures in each set is of interest, since the different functions in the bare vertices pick out different parts of the k -space. In this paper $t = 1$ serves as the energy unit; for the systems in mind we estimate²⁹ $t \sim .45$ eV.

In Fig. (1), we plot DC resistivity $\bar{\rho}_{xx}$ and Raman resistivities in the DC limit $\bar{\rho}_{A_{1g}}$, $\bar{\rho}_{B_{1g}}$, $\bar{\rho}_{B_{2g}}$ varying hole doping δ and fixing $t' = -0.2$. The four figures have roughly similar doping dependence, as suggested by the pseudo-identity. They all decrease when the doping increases, although the curvature changes more in $\bar{\rho}_{xx}$ and $\bar{\rho}_{A_{1g}}$ than the other two cases. This can be understood from Eq. (6) since they arise from the same kernel $\Upsilon(k, 0)$ with different filters. The quasi-particle peak in ρ_G , contributing most to $\Upsilon(k, 0)$, is located along the Fermi surface and gets broadened when warming up. The inset shows the corresponding squared vertex \mathcal{J}_α^2 in the background and the Fermi surfaces. The B_{1g} vertex vanishes along the line $k_x = k_y$ while the B_{2g} vertices vanish near $\{\pi, 0\}$ and $\{0, \pi\}$ points. In our calculation both B_{1g} and B_{2g} overlap well with the peak region of the spectral function, whereas A_{1g} and the resistivity do not. This

results in the difference between the T dependence of them and the other two in Fig. (1). It would be of considerable interest to study this pattern of T dependences systematically in future Raman studies.

Although all $\bar{\rho}_\alpha$ increase when reducing doping δ approaching the half-filling limit due to the suppression of quasi-particles, their magnitudes at high temperature vary considerably, as a result of different vertices filtering the contribution from $\Upsilon(k, 0)$. We can understand this scale difference by evaluating the average of vertices over the shaded region in Fig. (2). The shaded region covers the Fermi surface for all chosen δ and t' , and therefore contains the most significant contribution to ρ_α .

At $t' = -0.2$, $\langle \mathcal{J}_{xx}^2 \rangle_s \approx 2.41$, $\langle \mathcal{J}_{A_{1g}}^2 \rangle_s \approx 0.56$, $\langle \mathcal{J}_{B_{1g}}^2 \rangle_s \approx 1.30$, $\langle \mathcal{J}_{B_{2g}}^2 \rangle_s \approx 0.20$, where $\langle \rangle_s$ represents the k average over the shaded region. They not only explain the relation $\bar{\rho}_{xx} < \bar{\rho}_{B_{1g}} < \bar{\rho}_{A_{1g}} < \bar{\rho}_{B_{2g}}$, but also capture the ratio among them rather closely at high enough T. The structure at low T is more subtle, and carries information about the magnitude of t' that cannot be captured by the above high T argument.

Although all $\bar{\rho}_\alpha$ increase as δ decreases in general, their t' dependence can be rather different, as shown in Fig. (3). $\bar{\rho}_{xx}$ and $\bar{\rho}_{B_{1g}}$ decreases monotonically in general as t' increases from hole-doped (negative) to electron-

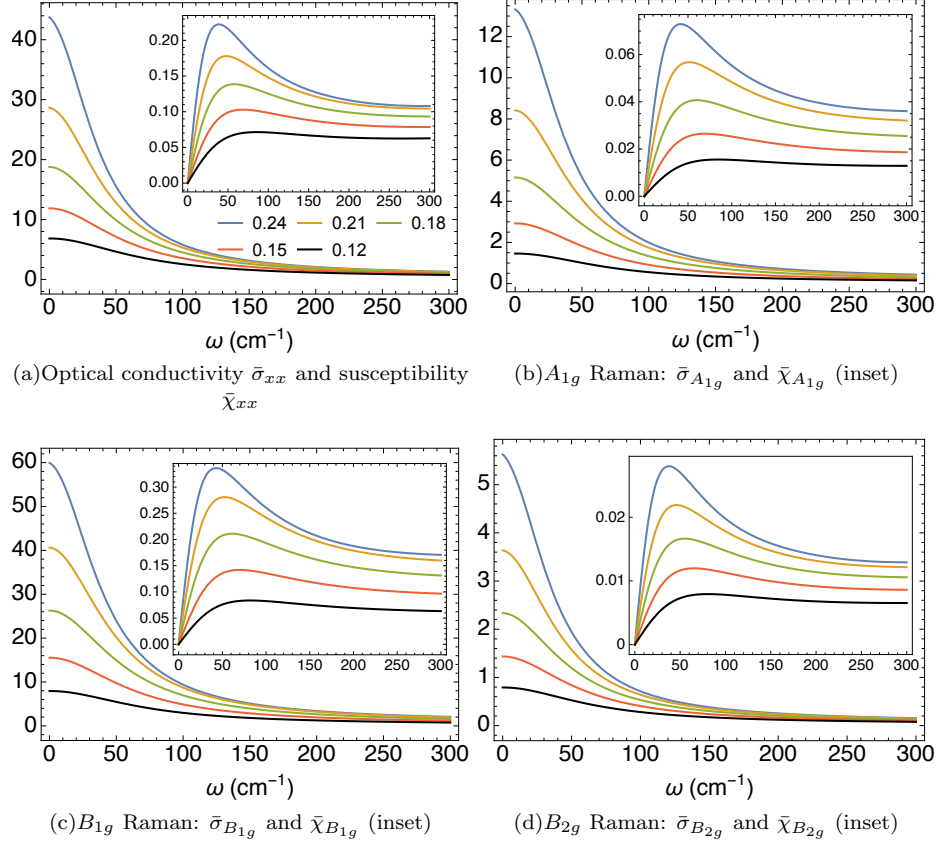


FIG. 4: Dynamical conductivities $\bar{\sigma}_\alpha$ and susceptibilities $\bar{\chi}_\alpha''$ (inset), for the hole doped case $t' = -0.2$, $T = 63\text{K}$ at different δ , as marked. In the experiments in Ref. [6] Fig. (1), the same quartet of results is shown for LSCO. At the highest energy of over 1000K, as in the data, the susceptibility shows no sign of dropping off.

doped (positive), while $\bar{\rho}_{A_{1g}}$ and $\bar{\rho}_{B_{2g}}$ decrease only as $|t'|$ increases and their monotonicity with respect to t' changes upon sign change of t' . Another interesting observation is that $\bar{\rho}_\alpha(t' = -0.2) > \bar{\rho}_\alpha(t' = 0.2)$ and $\bar{\rho}_\alpha(t' = -0.4) > \bar{\rho}_\alpha(t' = 0.4)$ are true for $\alpha = xx, B_{1g}$ and B_{2g} , but for the A_{1g} case, $\bar{\rho}_\alpha(t' = -0.2) < \bar{\rho}_\alpha(t' = 0.2)$ in general and $\bar{\rho}_\alpha(t' = -0.4) \approx \bar{\rho}_\alpha(t' = 0.4)$.

In Eq. (8), the resistivities depend on t' through $\Upsilon(k, 0)$ and \mathcal{J}_α^2 . To estimate their t' dependence, we can look at their average over the shaded region $\langle \Upsilon(k, 0) \rangle_s$ and $\langle \mathcal{J}_\alpha^2 \rangle_s$. While $\langle \Upsilon(k, 0) \rangle_s$ rises monotonically as t' increases, $\langle \mathcal{J}_\alpha^2 \rangle_s$ ($\alpha = xx, A_{1g}, B_{2g}$) is a quadratic function of t' which behaves differently at positive and negative t' , as shown in Eq. (2).

In the simplest B_{1g} case, $\mathcal{J}_{B_{1g}}^2$ is independent of t' . Then t' only affects $\bar{\rho}_{B_{1g}}$ through $\Upsilon(k, 0)$ and therefore $\bar{\rho}_{B_{1g}}$ increases almost monotonically as t' decreases (the crossing between $t = 0.2$ and $t = 0.4$ is due to the fact that the change on Fermi surface geometry leads to different filtering result when coupling to $\mathcal{J}_{B_{1g}}^2$). In the charge current case, the t' dependence of $\Upsilon(k, 0)$ still dominates since $\bar{\rho}_{xx}$ behaves similar to $\bar{\rho}_{B_{1g}}$ and the contribution from \mathcal{J}_{xx}^2 mostly modifies the curvature without affecting the relative scale.

The different behaviors in the other two cases indicate the quadratic t' dependence in \mathcal{J}_α^2 ($\alpha = A_{1g}, B_{2g}$) becomes dominant. In the simpler B_{2g} case, $\mathcal{J}_{B_{2g}}^2 \propto t'^2$ provides the dominant t' dependence in $\bar{\rho}_{B_{2g}}$, explaining $\bar{\sigma}_{B_{2g}}(t' = 0) = 0$ and $\bar{\rho}_{B_{2g}}(|t'| = 0.2) > \bar{\rho}_{B_{2g}}(|t'| = 0.4)$ regardless the sign of t' . Similarly due to quadratic t' dependence of $\mathcal{J}_{A_{1g}}^2$, $\bar{\rho}_{A_{1g}}(t' = 0) > \bar{\rho}_{A_{1g}}(|t'| = 0.2) > \bar{\rho}_{A_{1g}}(|t'| = 0.4)$.

Typically negative t' leads to stronger correlation and suppresses the quasi-particle peak²⁹ and hence for a certain $|t'|$, $\bar{\rho}_\alpha(t' < 0) > \bar{\rho}_\alpha(t' > 0)$ is generally true except for the A_{1g} case. In this exception, the negative linear t' term in $\mathcal{J}_{A_{1g}}^2$ shifts the stationary point away from $t' = 0$ and counters this effect from $\Upsilon(k, 0)$ for small $|t'|$ leading to $\bar{\rho}_{A_{1g}}(t' = -0.2) < \bar{\rho}_{A_{1g}}(t' = 0.2)$ and $\bar{\rho}_{A_{1g}}(t' = -0.4) \approx \bar{\rho}_{A_{1g}}(t' = 0.4)$.

Besides, $\bar{\rho}_{A_{1g}}$ shows rather different T -dependent behaviors between electron-doped $t' \geq 0$ and hole-doped $t' < 0$ cases. At negative t' , $\bar{\rho}_{A_{1g}}$ increases almost linearly with temperature. But at zero or positive t' , $\bar{\rho}_{A_{1g}}$ first increases sharply up to a certain temperature scale depending on t' and then crossovers to a region where the growth rate becomes much smaller.

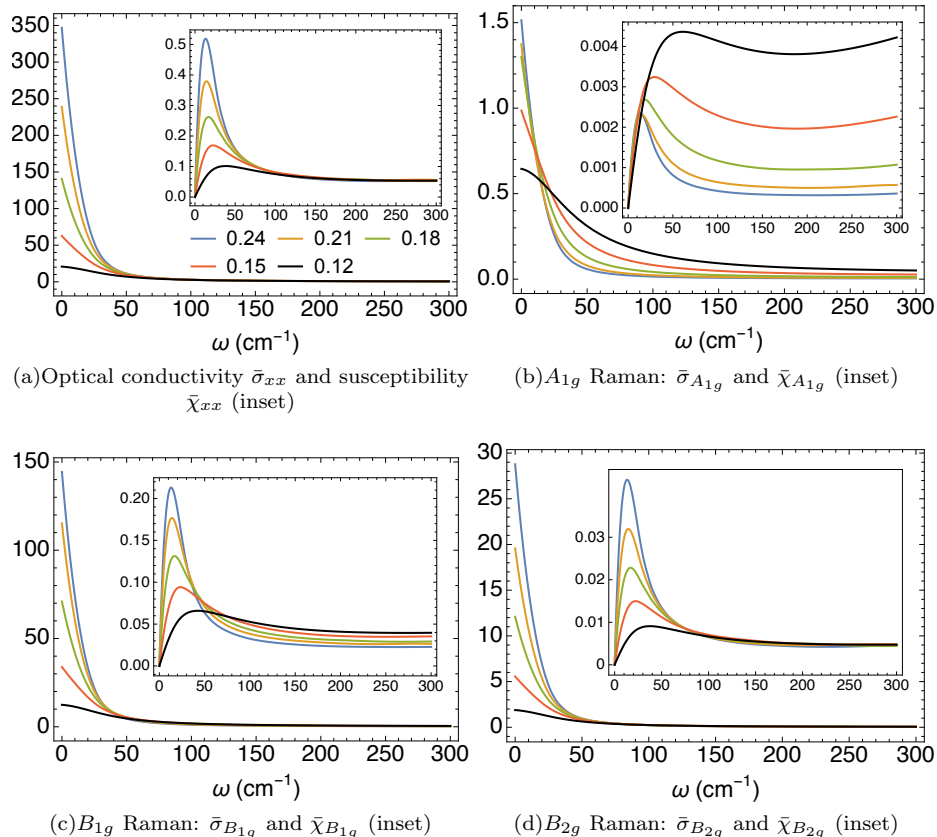


FIG. 5: Dynamical conductivities $\bar{\sigma}_\alpha$ and susceptibilities $\bar{\chi}''_\alpha$ (inset), for the electron doped case $t' = 0.2$, $T = 63\text{K}$ at different δ , as marked.

VI. FINITE ω RESULTS

Next we present the ω -dependent optical and Raman conductivities defined in Eq. (7). In Fig. (4) and Fig. (5), the set of four ω -dependent conductivities are displayed for the hole-doped system at $t' = -0.2$ and electron-doped system at $t' = 0.2$ respectively for a set of typical densities at a low T. In the insets we display the corresponding imaginary part of susceptibility, related through Eq. (6). In most cases, the quasi-elastic peak gets suppressed and shifts to higher frequency when reducing the carrier concentration. The only exception is $\bar{\chi}''_{A_{1g}}$ at $t' = 0.2$. Its quasi-elastic peaks are considerably smaller than other geometries due to the fluctuation in the specific vertex and get higher and broader as doping increases.

In Fig. (6) we focus on the electron doped case of varying T at $t' = 0.2$, $\delta = 0.15$ where high quality experimental results are available for the B_{2g} Raman channel in Ref. [10], see particularly Fig. (2). We evaluate the susceptibility at T values corresponding to those in this experiment. There is a fair similarity between theoretical curve (Panel (d)) and the experiment. In particular the theoretical curve reproduces the quasi-elastic peak, and its T evolution. The other three panels in Fig. (6) are

our theoretical predictions, they are equally amenable to experimental verification.

In the xx , B_{1g} , B_{2g} geometries, the quasi-elastic peaks in susceptibility get slightly higher and quite broader upon warming. The A_{1g} case is different. Its quasi-elastic peaks are much less obvious (too broad) except for the lowest temperature. And the peak magnitude is rather sensitive to temperature increase.

We also vary T at hole doping $t' = -0.2$ in Fig. (7). Comparing with the electron-doped case in Fig. (6), we note that the hole-doped optical and Raman objects share a greater similarity in shape dependence on T , if we ignore the scale difference. As T increases, the quasi-particle peaks get softened, and hence it generally suppresses the conductivities as well as the quasi-elastic peak in susceptibilities.

For completeness, the t' variation in $\bar{\sigma}_\alpha(\omega)$ and $\bar{\chi}''_\alpha(\omega)$ is plotted In Fig. (8), and looks rather different among various geometries. This can be understood as arising from the competition among various factors. We have a quadratic t' dependence in the squared vertices, a monotonic t' dependence in the magnitude and geometry of $\Upsilon(k, \omega)$. The t' dependence of the shape of $\bar{\sigma}_\alpha$ has more commonality. Another interesting observation is that, unlike the DC case when $\bar{\sigma}_{xx}$ and $\bar{\sigma}_{B_{1g}}$ are similarly af-

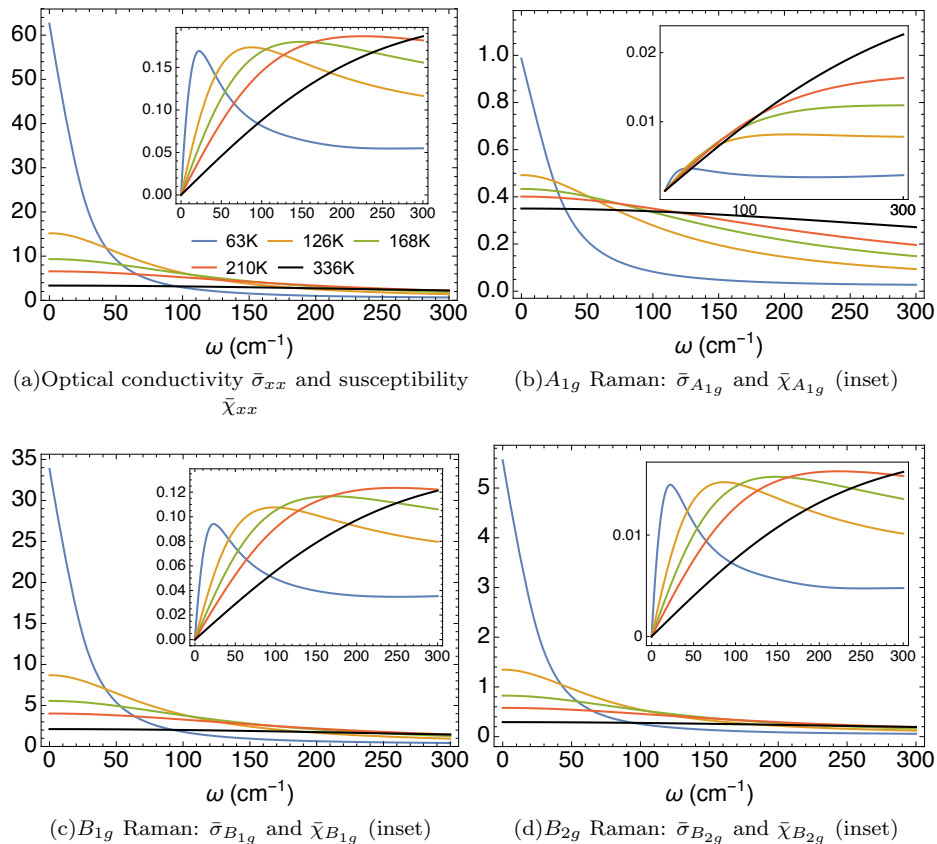


FIG. 6: Dynamical conductivities and (inset) susceptibilities for the electron doped case with $t' = 0.2$, $\delta = 0.15$, for various T 's as marked. Subfigure(d) with B_{2g} symmetry is comparable to the high resolution experimental result in Fig. (2) of Ref. [10] at comparable set of T 's. The theoretical curve reproduces well the quasi-elastic peaks, and their T evolution.

ected by t' , at finite frequency, their behaviors depend on t' rather differently. This difference is more obviously observed in terms of χ'' .

From the optical and Raman conductivities $\bar{\sigma}_\alpha$ we can extract a frequency scale Γ_α , as the half-width at half-maximum, in the unit of t . These are plotted against T in Fig. (9) for varying δ and Fig. (10) for varying t' . It is remarkable that despite a bare band width of ~ 3.6 eV, these frequency scales appear close to linear in T down to very low T . This is closely related to the observation in Ref. [29] that the resistivity departs from a T^2 behavior at extraordinarily low T 's, i.e. the effective Fermi temperatures are suppressed from the bare values by two or more orders of magnitude. Although the magnitude of the optical and Raman conductivities differs a lot, their relaxation rates describing the shape turn out to be much closer, as a result of similar T -dependent line shape of spectral function²⁹ in the normal state.

VII. CONCLUSION AND DISCUSSION

We have presented calculations of the electrical and Raman resistivities in the DC limit, the optical con-

ductivity, the Raman susceptibilities and related objects based on the second order ECFL theory in Ref. [29]. We computed the susceptibilities (using the leading order approximation) with the shown results. Experiments on different geometries can test and put some bound on this hypothesis of weak vertex corrections for the Raman operators. This is clearly of theoretical importance, since going beyond the bubble graphs brings in a formidable level of complexity.

The ECFL theory leads to a very small quasi-particle weight Z and a large background extending over the bandwidth, and has a very small effective Fermi temperature leading to interesting T dependence of the resistivity as discussed in²⁹. The line shape of the calculated Raman susceptibility is close to that for the case of electron doped NCCO Ref. [10] in terms of T and ω dependence, and therefore is promising. Our calculation also gives the Raman susceptibility in two other geometries, and this prediction can be checked against future experiments that are quite feasible. We note that the data Ref. [6] from Sugai *et al.* for this quartet of variables in the case of LSCO seems roughly consistent with our results, and a more detailed comparison is planned.

The focus on the T dependence in the $\omega \rightarrow 0$ limit, i.e.

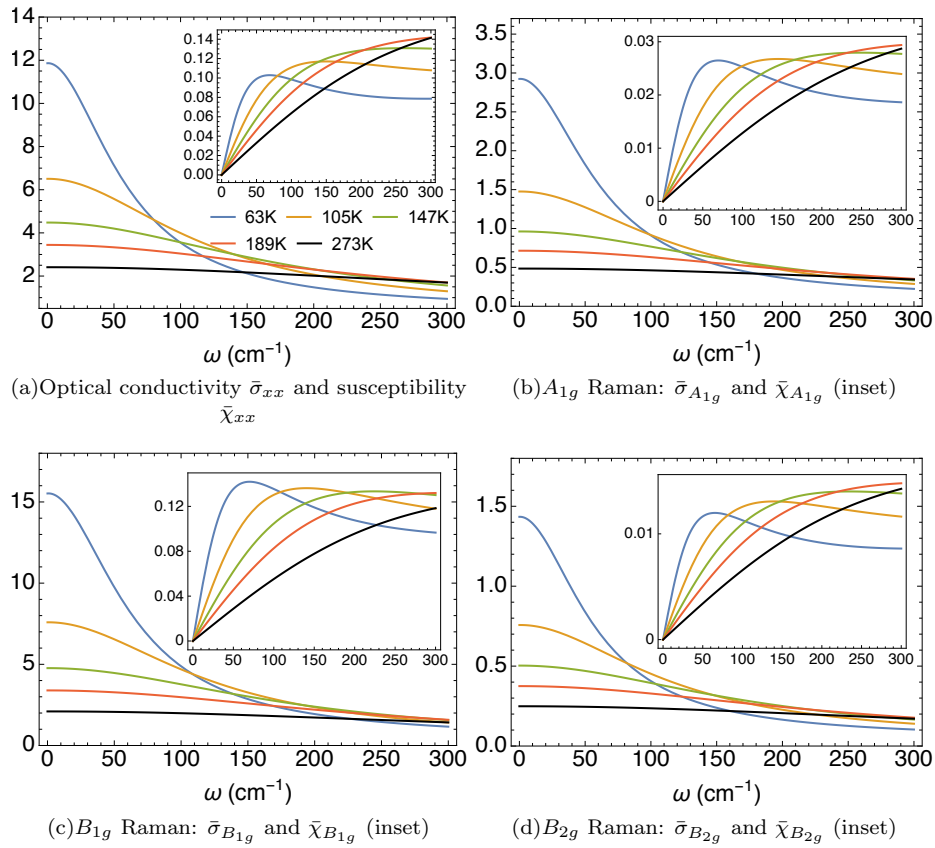


FIG. 7: Optical conductivity $\bar{\sigma}_{xx}(\omega)$ and the Raman conductivities $\bar{\sigma}_{A_{1g}}(\omega)$, $\bar{\sigma}_{B_{1g}}(\omega)$, $\bar{\sigma}_{B_{2g}}(\omega)$ at $t' = -0.2$, $\delta = 0.15$ and varying T , as marked (same legend for all subfigures). The corresponding dimensionless susceptibility is plotted in the inset with the same x-axis. Ref. [6], Ref. [7] and Ref. [10] show data that corresponds to these variables.

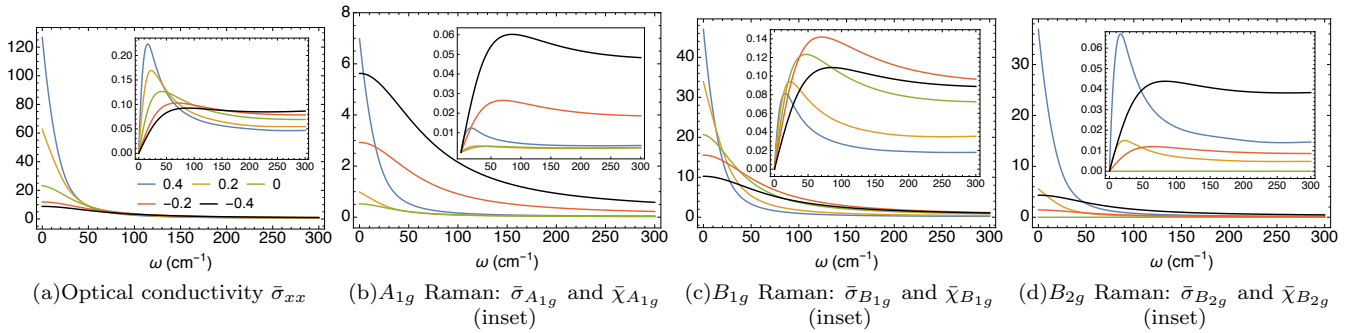


FIG. 8: Optical conductivity $\bar{\sigma}_{xx}(\omega)$ and the Raman conductivities $\bar{\sigma}_{A_{1g}}(\omega)$, $\bar{\sigma}_{B_{1g}}(\omega)$, $\bar{\sigma}_{B_{2g}}(\omega)$ at $\delta = 0.15$, $T = 63\text{K}$ and varying t' , as marked (same legend for all subfigures). The corresponding dimensionless susceptibility is plotted in the inset with the same x-axis. Ref. [6], Ref. [7] and Ref. [10] show data that corresponds to these variables.

on resistivities can be a quite fruitful goal for future experiments, since this limit gets rid of all excitations and measures the “pure-background”. It is an important exercise since the different geometries probe different combinations of t, t' as they occur in the bare vertices Eq. (2), as stressed above. We are predicting that the Raman resistivity in each channel can be found from the intensity at low T , and broadly speaking similar to resistivity. In

further detail, it is predicted to be (a) channel specific and (b) t'/t dependent. These clearcut predictions can be tested in future experiments.

Finally although such a measurement is not commonly done, a systematic measurement of the ratios of the scattering cross sections in different geometries should be feasible. These and the comparison between the quartet of susceptibilities presented here, can be profitably

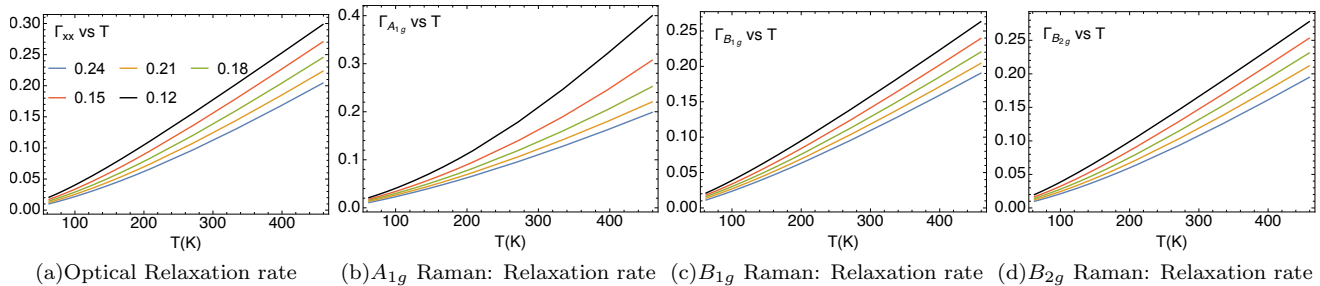


FIG. 9: Relaxation rates (half widths at half maximum) of $\sigma_\alpha(\omega)$ in units of t , at $t' = -0.2$ at various marked δ . The optical rate shows less convexity than the corresponding DC resistivity of Ref. [29]. The rates in (a,b) and in (c,d) have similar orders of magnitude, for reasons discussed in Fig. (1).

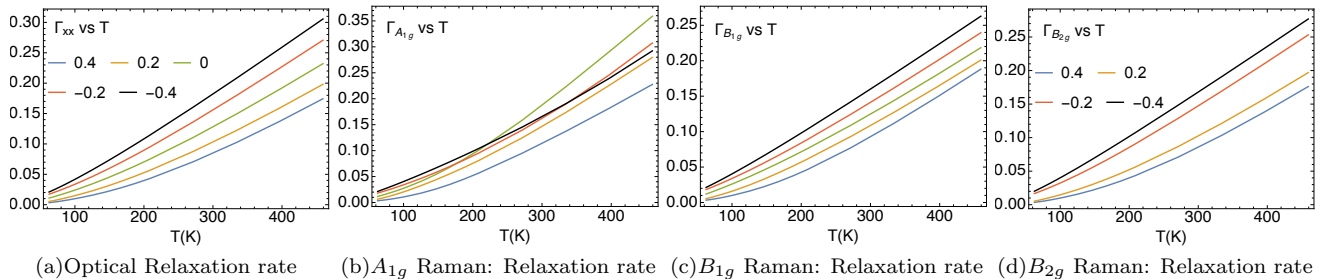


FIG. 10: The half-width at half-maximum for optical conductivity and Raman conductivities at $\delta = 0.15$ and varying t' , as marked.

compared with recent theories of strongly correlated systems to yield material parameters. Most importantly it can yield physical insights into the mechanism underlying the broad non-resonant Raman signals that have remained quite mysterious so far.

VIII. ACKNOWLEDGEMENT:

We thank Tom Devereaux, Lance Cooper and Girsh Blumberg for helpful discussions. The computation was

done on the comet in XSEDE³² (TG-DMR170044) supported by National Science Foundation grant number ACI-1053575. The work at UCSC was supported by the US Department of Energy (DOE), Office of Science, Basic Energy Sciences (BES), under Award No. DE-FG02-06ER46319.

¹ H. A. Kramers and W. Heisenberg, Z. für Physik, **31** 681 (1925).

² P. A. Wolff, Phys. Rev. **171**, 436 (1968).

³ P. A. Wolff and P. Platzmann, *Solid State Physics* (Academic, New York, 1973), Suppl. 13., W. Hayes and R. H. Loudon, *Scattering of Light by Crystals* (Wiley, New York, 1978).

⁴ A A Abrikosov and V M Genkin, Sov. Phys. JETP. **65**, 842 (1973).

⁵ S. Sugai, S. I. Shamoto and M. Sato, Phys. Rev. B **38**, 6436 (1988).

⁶ S. Sugai, Y. Takayanagi, N. Hayamizu, T. Muroi, J. Nohara, R. Shiozaki, K. Okazaki and K. Takenaka, Physica C **470**, S97 (2010).

⁷ S. Sugai, J. Nohara, R. Shiozaki, T. Muroi, Y. Takayanagi,

N. Hayamizu, K. Takenaka and K. Okazaki, J. Phys. C **25**, 415701 (2013).

⁸ R. Hackl, L. Tassini, F. Venturini, C. Hartinger, A. Erb, N. Kikugawa, and T. Fujita, in *Advances in Solid State Physics* **45**, 227 (2005).

⁹ M. M. Qazilbash, A. Koitzsch, B. S. Dennis, A. Gozar, H. Balci, C. A. Kendziora, R. L. Greene and G. Blumberg, Phys. Rev. B **72**, 214510 (2005).

¹⁰ A. Koitzsch, G. Blumberg, A. Gozar, B. S. Dennis, P. Fournier, and R. L. Greene, Phys. Rev. B **67** 184522 (2003).

¹¹ C. Sauer and G. Blumberg, Phys. Rev. B **82**, 014525 (2010).

¹² M. V. Klein and S. B. Dierker, Phys. Rev. B **29**, 4976 (1984).

- ¹³ M. V. Klein, S. L. Cooper, A. L. Kotz, R. Liu, D. Reznik, F. Slakey, W. C. Lee, D. M. Ginsberg, *Physica C* **185** 72 (1991). G. Blumberg and M V Klein, *J. Low. T. Phys. V* **117**, 1001 (1999).
- ¹⁴ F. Slakey, S. L. Cooper, M. V. Klein, J. P. Rice, and D. M. Ginsberg, *Phys. Rev. B* **39**, 2781(1989).
- ¹⁵ S. L. Cooper, D. Reznik, A. Kotz, M. A. Karlow, R. Liu, M. V. Klein, W. C. Lee, J. Giapintzakis, D. M. Ginsberg, B. W. Veal, and A. P. Paulikas, *Phys. Rev. B* **47** 8233 (1993).
- ¹⁶ S. L. Cooper, F. Slakey, M. V. Klein, J. P. Rice, E. D. Bukowski, and D. M. Ginsberg, *J. Opt. Soc. Am. B* **6** 436 (1989).
- ¹⁷ S. L. Cooper, M. V. Klein, B. G. Pazol, J. P. Rice, and D. M. Ginsberg, *Phys. Rev. B* **37** 5920 (1988).
- ¹⁸ B. S. Shastry and B. I. Shraiman, *Phys. Rev. Lett.* **65**, 1068 (1990).
- ¹⁹ B. S. Shastry and B. I. Shraiman, *Int. J. Mod. Phys. B* **5**, 365 (1991).
- ²⁰ J. K. Freericks, T. P. Devereaux, *Phys. Rev. B* **64**, 125110 (2001), J. K. Freericks, T. P. Devereaux, M. Moraghebi and S. L. Cooper, *Phys. Rev. Letts.* **94**, 216401 (2005).
- ²¹ T. P. Devereaux and R. Hackl, *Rev. Mod. Phys.* **79**, 175 (2007).
- ²² L. Medici, A. Georges, G. Kotliar, *Phys. Rev. B* **77**, 245128 (2008).
- ²³ J. Kosztin and A. Zawadowski, *Sol. St. Comm*, **78** 1029 (1991).
- ²⁴ B. S. Shastry, arXiv:1102.2858 (2011), *Phys. Rev. Letts.* **107**, 056403 (2011). <http://physics.ucsc.edu/~sriram/papers/ECFL-Reprint-Collection.pdf>
- ²⁵ B. S. Shastry and E. Perepelitsky, *Phys. Rev. B* **94**, 045138 (2016).
- ²⁶ B. S. Shastry, E. Perepelitsky and A. C. Hewson, arXiv:1307.3492, *Phys. Rev. B* **88**, 205108 (2013)
- ²⁷ P. Mai, S. R. White and B. S. Shastry, arXiv:1712.05396, *Phys. Rev. B* **98**, 035108 (2018).
- ²⁸ R. Žitko, D. Hansen, E. Perepelitsky, J. Mravlje, A. Georges and B. S. Shastry, arXiv:1309.5284, *Phys. Rev. B* **88**, 235132 (2013); E. Perepelitsky and B. S. Shastry, *Ann. Phys.* **338**, 283 (2013); B. S. Shastry and E. Perepelitsky, arXiv:1605.08213, *Phys. Rev. B* **94**, 045138 (2016).
- ²⁹ B. S. Shastry and P. Mai, *New J. Phys.* **20** 013027 (2018).
- ³⁰ P. Mai and B. S. Shastry, in preparation.
- ³¹ Parabolic bands leads to an exact cancellation, whereby the A_{1g} scattering is unobservable. Refs. ^{3,4,18,19} show that the cancellation is inoperative with non-parabolic bands, or with disorder. Experimentally Fig. (2) of Ref. [6] shows a A_{1g} contribution similar in scale to the other two geometries.
- ³² J. Town et al., “XSEDE: Accelerating Scientific Discovery”, *Computing in Science & Engineering*, Vol.16, No. 5, pp. 62-74, Sept.-Oct. 2014, doi:10.1109/MCSE.2014.80